CONSISTENT LDA′+DMFT APPROACH TO THE ELECTRONIC STRUCTURE OF TRANSITION METAL OXIDES: CHARGE TRANSFER INSULATORS AND CORRELATED METALS

I. A. Nekrasov ^{a*}, *N. S. Pavlov* ^{a}, *M. V. Sadovskii* ^{a,b}

^{a} *Institute for Electrophysics, Ural Branch, Russian Academy of Sciences*
620016, Ekaterinburg, Russia

^{b} *Institute for Metal Physics, Ural Branch, Russian Academy of Sciences*
620990, Ekaterinburg, Russia

We discuss the recently proposed LDA′+DMFT approach providing a consistent parameter-free treatment of the so-called double counting problem arising within the LDA+DMFT hybrid computational method for realistic strongly correlated materials. In this approach, the local exchange-correlation portion of the electron–electron interaction is excluded from self-consistent LDA calculations for strongly correlated electronic shells, e. g., d-states of transition metal compounds. Then, the corresponding double-counting term in the LDA′+DMFT Hamiltonian is consistently set in the local Hartree (fully localized limit, FLL) form of the Hubbard model interaction term. We present the results of extensive LDA′+DMFT calculations of densities of states, spectral densities, and optical conductivity for most typical representatives of two wide classes of strongly correlated systems in the paramagnetic phase: charge transfer insulators (MnO, CoO, and NiO) and strongly correlated metals ($SrVO_3$ and Sr_2RuO_4). It is shown that for NiO and CoO systems, the LDA′+DMFT approach qualitatively improves the conventional LDA+DMFT results with the FLL type of double counting, where CoO and NiO were obtained to be metals. Our calculations also include transition-metal $4s$-states located near the Fermi level, missed in previous LDA+DMFT studies of these monooxides. General agreement with optical and the X-ray experiments is obtained. For strongly correlated metals, the LDA′+DMFT results agree well with the earlier LDA+DMFT calculations and existing experiments. However, in general, LDA′+DMFT results give better quantitative agreement with experimental data for band gap sizes and oxygen-state positions compared to the conventional LDA+DMFT method.

1. INTRODUCTION

During last decade, the LDA+DMFT method (local density approximation + dynamical mean-field theory) became probably the most powerful tool for calculating electronic structure of real strongly correlated materials [1–7]. This approach typically consists of two computation steps. First, LDA calculations are used to obtain the noninteracting Hamiltonian $\hat{H}^{LDA}$ that rather accurately describes the kinetic energy (and to some extent takes electronic interactions into account). Second, the local Coulomb (Hubbard) interaction $\hat{H}^{Hub}$ is introduced into the lattice problem de-

fined by $\hat{H}^{LDA}$ for those electronic shells that are supposed to be strongly correlated. A generalized Hubbard model thus obtained is solved numerically using DMFT. Some attempts to organize a feedback from the DMFT step to LDA calculations to achieve a fully self-consistent LDA+DMFT method are also known and may be important for some physical problems [8].

The double counting problem arises in the standard LDA+DMFT method because some part of the local electron–electron interaction for correlated shells is actually accounted for by $\hat{H}^{LDA}$. To avoid this double counting, it is necessary to subtract a certain correction term $\hat{H}^{DC}$ from $\hat{H}^{LDA}$. Then, the formal LDA+DMFT Hamiltonian is written as

$$\hat{H} = \hat{H}^{LDA} + \hat{H}^{Hub} - \hat{H}^{DC}. \tag{1}$$

In orbital space, $\hat{H}^{DC}$ is the diagonal matrix with

*E-mail: nekrasov@iep.uran.ru

nonzero and equal matrix elements E_{dc} for the atomic shells that are assumed to be strongly correlated (e. g., d or f shells or their subshells). This becomes more transparent if we consider the corresponding Green's function for the Hubbard model:

$$\hat{G}_{ij}(\mathbf{k}E) = \Big[(E - \mu)\hat{I} - H_{ij}^{LDA}(\mathbf{k}) -$$
$$- \big(\Sigma(\mathbf{k}E) - E_{dc} \big) \delta_{id}\delta_{jd} \Big]^{-1}, \quad (2)$$

where $\hat{I}$ is the unit matrix in the orbital space, μ is the chemical potential, $\Sigma(\mathbf{k}E)$ is the self-energy corresponding to the local Coulomb (Hubbard) interaction, $[\dots]^{-1}$ denotes matrix inversion, and the index d denotes correlated states for which the Coulomb (Hubbard) interaction is taken into account.

It follows from Eq. (2) that if $\hat{H}^{LDA}$ contains only the contribution of interacting d-orbitals, E_{dc} reduces to a trivial renormalization of the chemical potential μ. Then, strictly speaking, there is no double counting problem at all. Because of this many of the early works (listed, e. g., in reviews [2, 4–7]), except, probably, the first paper on LDA+DMFT [1] and a few others, just dropped the double-counting correction term. Only after the LDA+DMFT community started active studies of multiband $\hat{H}^{LDA}$ Hamiltonians with both correlated and noncorrelated states included, the problem of the correct implementation of $\hat{H}^{DC}$ became important. Now, there are dozens of works devoted to multiband LDA+DMFT studies. Important classes of materials investigated can be listed as follows.

1. Transition metal oxides (LaTiO$_3$, (Sr,Ca)VO$_3$, V$_2$O$_3$, VO$_2$, CrO$_2$, LaMnO$_3$, NiO, MnO, CoO, FeO, LaCoO$_3$, TiOCl, Tl$_2$Mn$_2$O$_7$, LaNiO$_3$, (Ca,Sr)$_2$RuO$_4$, and Na$_{0.3}$CoO$_2$).

2. Elemental transition metals and nonoxide transition metal compounds (Cr, Mn, Fe, Ni, Co, multilayers (CrAs)/(GaAs), NiMnSb, Co$_2$MnSi, CrAs, VAs, ErAs, Ni(S,Se)$_2$, and KCuF$_3$).

3. Elemental f-electron materials and their compounds (Ce, Pu, Am, Ce$_2$O$_3$, Pu$_2$O$_3$, USe, UTe, PuSe, PuTe, PuCoGa$_5$, URu$_2$Si$_2$, CeIrIn$_5$, CeCoIn$_5$, and CeRhIn$_5$).

4. Nanomaterials (Ni–Cu nanocontacts and nanoelectrodes).

5. High-temperature copper superconductors ((Sr,La)$_2$CuO$_4$, (Pr,Ce)$_2$CuO$_4$, Bi$_2$Ca$_2$SrCuO$_8$, etc.).

6. Superconducting iron pnictides (LaFeAsO, CeFeAsP, LiFeAs, BaFe$_2$As$_2$, etc.).

These systems show a large variety of physical effects. Among them, there are strongly correlated metals, Mott and charge transfer insulators, ferromagnets and antiferromagnets, superconductors, etc. However,

there is currently no universal and unambiguous expression for $\hat{H}^{DC}$, and different formulations are used for different classes of materials.

In this paper, we present the results of extensive application of our recently proposed LDA$'$+DMFT approach [13] to charge-transfer insulators MnO, CoO, and NiO and strongly correlated metals SrVO$_3$ and Sr$_2$RuO$_4$, confronted to conventional LDA+DMFT results and some experiments. The paper has the following structure. In Sec. 2, we present an overview of different definitions of $\hat{H}^{DC}$. The novel consistent LDA$'$+DMFT method is described in Sec. 3. LDA and LDA$'$ band structures, total and partial densities of states, and spectral density maps and optical conductivity LDA$'$+DMFT results for prototype charge transfer insulators MnO, NiO, and CoO are presented in Sec. 4 and are compared with the results of the conventional LDA+DMFT approach. These results are further compared with experimental data on X-ray spectroscopy and optical conductivity. In Sec. 5, we discuss LDA and LDA$'$ band structures for correlated metallic system prototypes SrVO$_3$ and Sr$_2$RuO$_4$. Then, the LDA+DMFT and LDA$'$+DMFT results are compared with each other and with experimental photoemission and absorption spectra. We end with the conclusions in Sec. 6.

2. REVIEW OF DIFFERENT FORMULATIONS FOR $\hat{H}^{DC}$

To derive an expression for $\hat{H}^{DC}$, we examine the $\hat{H}^{LDA}$ and $\hat{H}^{Hub}$ terms in Eq. (1). The LDA part of Hamiltonian (1) is given by

$$\hat{H}_{LDA} = -\frac{\hbar^2}{2m_e}\Delta + V_{ion}(\mathbf{r}) +$$
$$+ \int d^3r' \, \rho(\mathbf{r}')V_{ee}(\mathbf{r} - \mathbf{r}') + \frac{\delta E_{xc}^{LDA}(\rho)}{\delta\rho(\mathbf{r})}, \quad (3)$$

where Δ is the Laplace operator, m_e the electron mass, e the electron charge, and

$$V_{ion}(\mathbf{r}) = -e^2 \sum_i \frac{Z_i}{|\mathbf{r} - \mathbf{R_i}|},$$
$$V_{ee}(\mathbf{r} - \mathbf{r}') = \frac{e^2}{2} \sum_{\mathbf{r} \neq \mathbf{r}'} \frac{1}{|\mathbf{r} - \mathbf{r}'|} \quad (4)$$

are respectively the one-particle potential due to all ions i with charges eZ_i at given positions $\mathbf{R_i}$, and the electron–electron interaction.

The $E_{xc}^{LDA}(\rho(\mathbf{r}))$ term in Eq. (3) is a function of the local charge density and approximates the true

exchange correlation functional $E_{xc}[\rho]$ of the density functional theory within the local density approximation [9]. The explicit expression for $E_{xc}^{LDA}(\rho(\mathbf{r}))$ is usually derived from the perturbation theory [10] or numerical simulations [11] of the "jellium" model with $V_{ion}(\mathbf{r}) = \text{const}$. Obtaining the value of the local charge density requires choosing some basis set of one-particle wave functions φ_i (e. g., performing practical calculations and explicitly expressing matrix elements of Hamiltonian (3)), in terms of which $\rho(\mathbf{r})$ is written as

$$\rho(\mathbf{r}) = \sum_{i=1}^{N} |\varphi_i(\mathbf{r})|^2. \quad (5)$$

The Hubbard-like (local) interaction term including the direct Coulomb interaction and exchange Coulomb interaction contributions in the density–density form is written as

$$\hat{H}^{Hub} = U \sum_{m} \sum_{i} \hat{n}_{im\uparrow}\hat{n}_{im\downarrow} + $$
$$+ \sum_{i} \sum_{m\neq m'} \sum_{\sigma\sigma'} (U' - \delta_{\sigma\sigma'} J)\, \hat{n}_{im\sigma}\hat{n}_{im'\sigma'}, \quad (6)$$

where the index i enumerates lattice sites, m denotes orbitals, and σ the spin; U represents the local intra-orbital Coulomb repulsion and J is the z-component of Hund's rule coupling between the strongly correlated electrons (e. g., d-states, enumerated by $i = i_d$ and $l = l_d$). Rotational invariance then fixes the local inter-orbital Coulomb repulsion $U' = U - 2J$ [12]. The values of U and J are usually obtained from constrained LDA [16] or constrained RPA (random phase approximation) [17] procedures. A numerically exact solution of the Hubbard Hamiltonian (a simplified kinetic term plus the $\hat{H}^{Hub}$ term) can be obtained within the DMFT approximation.

The Hamiltonian $\hat{H}_{LDA}$ contains local electron–electron correlations through the exchange correlation energy (taken in the form valid for a homogeneous electronic gas) and the density–density contribution of the Hartree term. In its turn, DMFT provides the numerical solution of the Hubbard model (exact in infinitely many dimensions). It is therefore clear that before substituting $\hat{H}_{LDA}$ in DMFT lattice problem (2), we must subtract certain double-counting correction term $\hat{H}^{DC}$ from $\hat{H}_{LDA}$. The double counting problem arises because there is no explicit microscopic or diagrammatic relation between the model (Hubbard-like) Hamiltonian approach and the LDA. There is apparently no possibility to give a rigorous expression for $\hat{H}^{DC}$ in terms of U, J, and ρ. Several *ad hoc* expressions

for $\hat{H}^{DC}$ and approaches to treat the double counting problem exist in the current literature. Below, we briefly discuss some of these derivations.

Perhaps for the first time, the problem of double counting occurred in an attempt to merge the LDA and the Hubbard model within the LDA+U method [14], where the so-called "around mean-field" (AMF) definition of $\hat{H}^{DC}$ was initially postulated. This definition comes from the assumption that the LDA is a kind of "mean-field" solution of the Hubbard-like problem in Eq. (6). The definition in Ref. [14] was subsequently generalized to the spin-dependent (LSDA) case (and even more generally to the matrix form of Coulomb interaction). After this, the spin-dependent generalization of the corresponding AMF expression can be given as

$$\hat{H}_{AMF}^{DC} = \frac{1}{2}U \sum_{\sigma} n_{d\sigma}(n_d - n_\sigma^0) - $$
$$- \frac{1}{2}J \sum_{\sigma} n_{d\sigma}(n_{d\sigma} - n_\sigma^0) \quad (7)$$

with the average occupancies

$$n^0 = \frac{1}{2(2l+1)} \sum_{m,\sigma} n_{m\sigma}, \quad n_\sigma^0 = \frac{1}{(2l+1)} \sum_{m} n_{m\sigma}$$

and the total number of electrons on interacting orbitals (per spin projection)

$$n_{d\sigma} = \sum_{m} n_{il_d m\sigma} = \sum_{m} \langle \hat{n}_{il_d m\sigma} \rangle$$

and $n_d = \sum_{\sigma} n_{d\sigma}$, originally supposed to be found from LDA calculations. The drawback of the AMF is the equal occupancy of all orbitals, which is not correct even for weakly correlated systems because, e. g., of crystal field splitting. However, a couple of the modern LDA+DMFT works reported reasonable results with an AMF-like double-counting correction term. Apparently, the AMF double counting correction works rather well for moderately correlated metallic systems. Some modifications of Eq. (7) were given in Refs. [18] and applied to LDA+DMFT calculations for charge-transfer insulators.

Later on, the fully localized (or atomic) limit (FLL) expression for $\hat{H}^{DC}$ was introduced in Refs. [15, 19] (with the first application to LDA+DMFT calculations in Ref. [1]):

$$\hat{H}_{FLL}^{DC} = \frac{1}{2}Un_d(n_d - 1) - \frac{1}{2}J \sum_{\sigma} n_{d\sigma}(n_{d\sigma} - 1). \quad (8)$$

Equation (8) actually represents the Hartree decoupling of Hubbard-model interaction term (6): the decoupling of the density–density term $\hat{n}_i\hat{n}_j$ and not the

full four-operator term $\hat{c}_i^\dagger \hat{c}_j^\dagger \hat{c}_o \hat{c}_l$. Hence, strictly speaking, there is no Fock-type contribution in Eq. (8) because Hund exchange is represented in Eq. (6) in the density–density form, although Hund coupling value J has the "exchange nature". It is quite often misinterpreted as being due to the "true" Hartree–Fock decoupling of the $\hat{c}_i^\dagger \hat{c}_j^\dagger \hat{c}_o \hat{c}_l$ term.

The FLL expression in the context of LDA+DMFT calculations was used in the majority of modern works. It works reasonably well for both metallic and insulating strongly correlated materials. Recently, some modifications of the FLL were proposed in Refs. [20, 21]. These modifications are typically used for quantitative improvements of LDA+DMFT results for particular compounds. Some kind of an AMF and FLL "hybrid scheme" was used in Ref. [22] for α-Fe.

An alternative way to derive or guess the $\hat{H}^{DC}$ term is to express it through the characteristics of an intrinsic DMFT single-impurity problem, such as the impurity self-energy $\Sigma_{mm'}^{imp}$ or the impurity Green's function $G_{mm'}^{imp}$. A popular way is to define the doubly counted energy as the static part of the impurity self-energy [23]:

$$E_{dc} = \frac{1}{2} \mathrm{Tr}_\sigma \left(\Sigma_\sigma^{imp}(0) \right). \qquad (9)$$

Some LDA+DMFT papers used this definition in calculations of metallic magnetic and nonmagnetic systems. From the very beginning, this type of double counting correction was also exploited within the GW+DMFT approach [24].

The Hartree energy can be determined from the LDA+DMFT self-energy as its real part in the high-frequency limit. In Ref. [27], it was proposed to use the Hartree energy thus defined as a double counting correction, using the constraint

$$\mathrm{Re}\,\mathrm{Tr}\left(\Sigma_{mm'}^{imp}(i\omega_N) \right) = 0, \qquad (10)$$

where ω_N is the highest Matsubara frequency used in calculations. A physically similar definition of the double counting term $E_{dc} = \Sigma(\omega \to \infty)$ was successfully applied to metallic ferromagnet $SrCoO_3$ in Ref. [25].

For metallic systems, it was suggested to fix the double counting correction by equating the numbers of particles in the noninteracting problem and in the impurity problem, expressed via the corresponding Green's functions [26]:

$$\mathrm{Tr}\ G_{mm'}^{imp}(\beta) = \mathrm{Tr}\ G_{mm'}^{0,loc}(\beta), \qquad (11)$$

where $G_{mm'}^{0,loc}$ is the local noninteracting Green's function. Some LDA+DMFT works treated the double

counting energy E_{dc} as a free parameter. The authors of Ref. [27] found that most of the $\hat{H}^{DC}$ terms proposed in the literature are not completely satisfactory in the case of charge transfer insulator NiO and proposed a numerical way to define the necessary double counting correction.

Another possible solution of the double counting problem is to perform Hartree+DMFT or Hartree–Fock+DMFT calculations [28]. In performing Hartree–Fock band-structure calculations for real materials, we do exactly know what portion of interaction is included. Because diagrammatic expressions for the Hartree or Hartree–Fock terms are well known, one can calculate them directly and obtain the double counting correction energy explicitly. However, we are unaware of any Hartree+DMFT or Hartree–Fock+DMFT calculations for real materials.

A totally independent branch of *ab initio* DMFT calculations is the GW+DMFT method, where, instead of the density functional theory, the so called chain of Hedin equations is used, truncated in a simplest manner by neglecting vertex corrections (see Ref. [24, 29] for a review). Because of the purely diagrammatic nature of the GW method, there is a natural way to calculate the local part of the corresponding Hartree contribution, which can be used as the double counting correction term for GW+DMFT [29].

3. CONSISTENT LDA′+DMFT APPROACH

Recently, we proposed the LDA′+DMFT approach, which defines a consistent parameter-free way to avoid the double counting problem [13]. The main idea is to explicitly exclude the exchange-correlation energy from self-consistent LDA calculations only for correlated bands. As described above, the main obstacle to expressing the double counting term exactly is the exchange-correlation $E_{xc}^{LDA}(\rho(\mathbf{r}))$ portion of interaction within the LDA. It therefore seems somehow inconsistent to use it to describe correlation effects in narrow (strongly correlated) bands from the very beginning, because these should be treated via more elaborate schemes like DMFT. To overcome this difficulty for these states, we propose to redefine charge density (5) in E_{xc}^{LDA} as

$$\rho'(\mathbf{r}) = \sum_{i \neq i_d} |\varphi_i(\mathbf{r})|^2, \qquad (12)$$

excluding the contribution of the density of strongly correlated electrons.

In principle, E_{xc}^{LDA} is not an additive function of charge density. Hence, splitting the charge density into

two parts may lead to some loss of hybridization between correlated and uncorrelated states. However, as we show below, this approximation is rather good. We see in what follows that LDA′ bands practically do not change their shape with respect to LDA ones for all considered systems. This suggests that "hybridization" is almost unaffected by LDA′. The main effect is an increase in the splitting between oxygen $2p$ and metal $3d$ states. It comes from the more repulsive potential appearing in the LDA′ case because part of the exchange correlation energy is then excluded.

The redefined $\rho'(\mathbf{r})$ in Eq. (12) is next used to obtain E_{xc}^{LDA} and perform self-consistent LDA′ band structure calculations for correlated bands. Just the Hartree contribution, Eq. (3), to the interaction for correlated states is then left at the LDA′ stage. The double counting correction term should therefore be consistently taken in the form of the Hartree-like term in Eq. (8). This definition of H_{FLL}^{DC} also does not have any free parameters. Actually, our approach is in precise correspondence with the standard definition of correlations as interaction corrections "above" the Hartree–Fock level. At the same time, all other states (not counted as strongly correlated) are to be treated with the full power of DFT/LDA and the full ρ in E_{xc}^{LDA}.

Although the LDA′+DMFT method is apparently most consistent with the use of the FLL type of double counting, in principle all definitions of H^{DC} mentioned above can also be used within LDA′+DMFT. Also, there is another "degree of freedom left": the occupancy n_d used in the FLL equation, either can be obtained from LDA or LDA′ results, or can be calculated self consistently during the DMFT loop. We used all these variants in our calculations for different compounds presented below. The corresponding values of E_{dc} are listed in Table. We use the notation FLL(SC) for the self-consistently calculated n_d and FLL(LDA) for n_d calculated from LDA or LDA′. In general, the FLL(SC) and FLL(LDA) results do not differ very much from each other, except for the case of CoO (see below). However, the FLL(SC) calculation gives a slightly better agreement with experiments. Most Figures presented below are plotted for the FLL(SC) case. We observed that FLL(SC) calculations require more computational time than FLL(LDA) ones.

Therefore, our consistent LDA′+DMFT approach is a kind of compromise between Hartree–Fock and DFT/LDA starting points to be followed by DMFT calculations. It was demonstrated in Ref. [13] that this LDA′+DMFT method works perfectly for the insulating NiO system, directly producing the charge-transfer
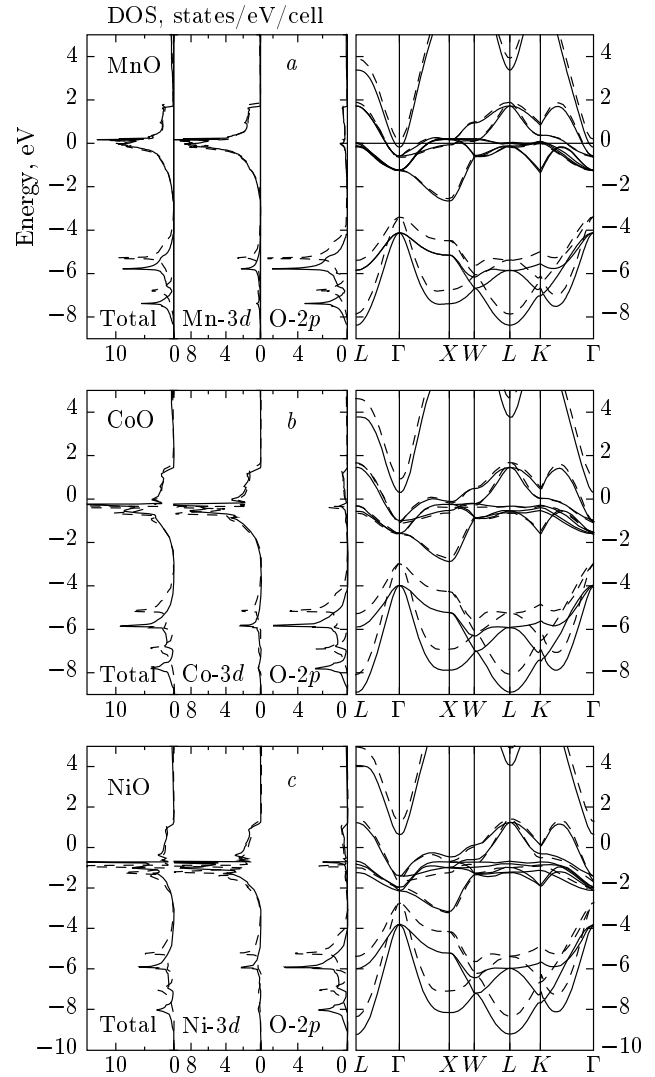

Fig. 1. LDA (dashed lines) and LDA′ (solid lines) densities of states (DOS) and band dispersions for MnO (a), CoO (b), and NiO (c). The Fermi level is zero

insulator solution, while the conventional LDA+DMFT method (with FLL) gives a metallic solution (cf. Ref. [27]).

4. CHARGE-TRANSFER INSULATORS

4.1. LDA and LDA′ band structures

Typical examples of charge-transfer insulator (CTI) materials are transition metal monoxides MnO, CoO, and NiO. These oxides have a rock salt crystal structure with the respective lattice parameters $a = 4.426$ Å, 4.2615 Å, 4.1768 Å. To obtain LDA and LDA′ band structures for MnO, CoO, and NiO, the basis set of lin-

Table. LDA and LDA′ occupancies and the corresponding values of the LDA+DMFT and LDA′+DMFT double-counting terms (eV) for systems under consideration

Compound	n_{LDA}	$n_{LDA'}$	LDA+DMFT FLL(LDA)	LDA+DMFT FLL(SC)	LDA′+DMFT FLL(LDA)	LDA′+DMFT FLL(SC)
SrVO$_3$	2.61	2.44	12.33	11.99	10.35	10.92
Sr$_2$RuO$_4$	5.65	5.39	14.32	14.60	12.92	13.73
MnO	5.59	5.43	39.05	35.49	36.62	35.30
CoO	7.60	7.41	54.28	50.90	51.42	50.49
NiO	8.54	8.34	60.90	62.01	57.91	58.13

earized muffin-tin orbitals (LMTO) [30] was used. In the corresponding program package TB-LMTO v.47, E_{xc}^{LDA} was taken in the von Barth–Hedin form [10]. Total and partial densities of states (DOS) together with band dispersions can be seen in Fig. 1 for LDA (dashed lines) and LDA′ (solid lines). Figure 1 shows MnO, CoO, and NiO systems from top down. As reported earlier for NiO [13], the LDA′ approach changes the charge transfer energy $|E_d - E_p|$, where E_d and E_p are, roughly speaking, one-electron energy positions of transition-metal $3d$ and O-$2p$ bands. In Fig. 1, the same tendency for MnO and CoO oxides can be seen. For MnO, it increases by about 0.5 eV and for CoO, by about 1 eV, similar to NiO. An almost rigid shift of the O-$2p$ bands down in energy is observed here, while transition-metal $3d$ states remain almost the same near the Fermi level.

We note that to our knowledge, transition-metal $4s$ states have never been included into LDA+DMFT calculations for these transition metal oxides. Apparently, this was because they were reasonably assumed to be weakly correlated and thus projected out from the corresponding LDA Hamiltonian. But the transition-metal $4s$ states are rather close to the Fermi level for LDA bands and even closer for LDA′ ones. They can be seen in Fig. 1 as lowest unoccupied states that touch the Fermi level near the Γ point for MnO and less than 1 eV above the Fermi level for CoO and NiO.

4.2. LDA+DMFT and LDA′+DMFT spectral functions

Everywhere in this paper, we use the Hirsh–Fye quantum Monte Carlo algorithm [31] as the impurity solver for DMFT equations. To set up a DMFT lattice problem, we use corresponding LDA and LDA′ Hamiltonians, which include all states (without any projec-

tion, as was done, e. g., in Ref. [26]). The inverse temperature was chosen as $\beta = 5$ eV^{-1}, with 80 time slices for NiO, and $\beta = 10$ eV^{-1} with 120 and 160 time slices for MnO and CoO respectively. Monte Carlo sampling was done with 10^6 sweeps. The use of rather high temperatures does not lead to any qualitative effects in the results, which allows avoiding unnecessary computational efforts. The Coulomb interaction parameters were chosen typical for MnO, CoO, and NiO [18, 27]: $U = 8$ eV and $J = 1$ eV. Both FLL(SC) and FLL(LDA) double counting definitions were applied for all materials. The corresponding E_{dc} values are given in the Table.

To obtain DMFT(QMC) densities of states (DOS) at real energies, we used the maximum-entropy method (MEM) [32]. The DMFT self-energy can then be obtained on the real frequency axis by using Pade approximants for the analytical continuation. We subsequently checked that "Pade" DOS are identical to the "MEM" ones. Once $\Sigma(\omega)$ is obtained, we can input it into Eq. (2) and obtain the spectral density function

$$A(\mathbf{k}, \omega) = -\frac{1}{\pi} \operatorname{Im} G(\mathbf{k}, \omega).$$

The corresponding maps of spectral density functions, representing the effective band structure of these compounds, are given in Fig. 2.

The left column in Fig. 2 presents LDA+DMFT results and the right one presents the LDA′+DMFT results for MnO (upper panels), CoO (middle panels), and NiO (lower panels).

4.3. LDA+DMFT and LDA′+DMFT DOS

In Fig. 3, we present densities of states obtained by the LDA+DMFT (dashed lines) and LDA′+DMFT (solid lines) methods. The left panel corresponds to
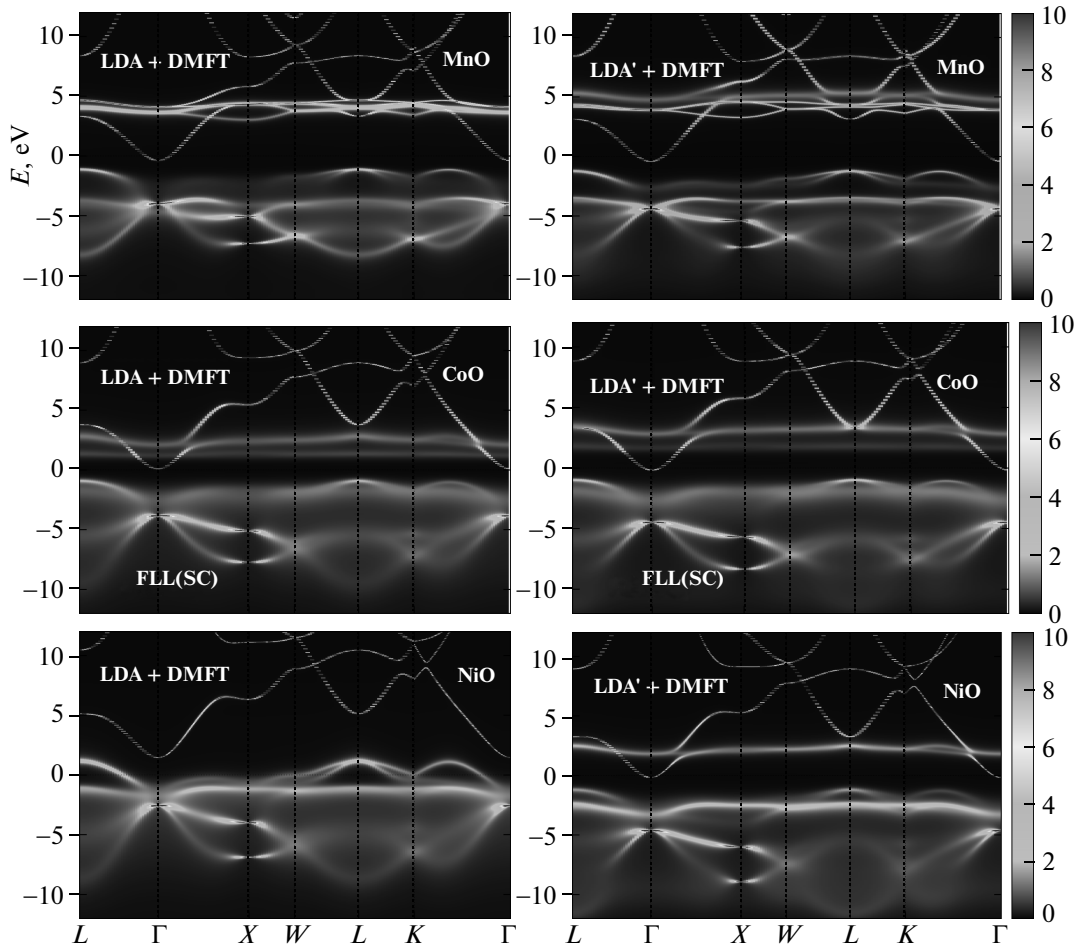
Fig. 2. Comparison of LDA+DMFT (left column) and LDA′+DMFT (right column) calculated spectral density functions for MnO (upper row), CoO (middle row), and NiO (lower row), with the FLL(SC) double-counting correction. The Fermi level is zero

MnO, the middle one to CoO, and the left one to NiO. The top row shows total densities of states, while other rows show the contributions of the most important electron states, the t_{2g} and e_g subshells for a $3d$ transition metal, oxygen $2p$ states, and transition-metal $4s$ states.

We first focus on the MnO case, which is perhaps the simplest among these three. The O-$2p$ states are located between -9 eV and -4 eV (see Figs. 2 and 3). Then comes the lower Hubbard band (LHB), which consists of the respective Mn-$3d$ t_{2g} and e_g contributions at -4 eV and -2.3 eV. On the plots of the spectral-function, LHB is a rather wide nondispersive band at these energies. Then we see the so-called Zhang–Race band — the bound state that appears when a strongly interacting band is hybridized with the charge reservoir. This band can be seen as a peak at -1.5 eV in O-$2p$ states together with Mn-$3d$ e_g

states. Then, between the Zhang–Race band and the upper Hubbard band (UHB), there is a gap for Mn-$3d$ states of about 3.5 eV in both LDA+DMFT and LDA′+DMFT lases, which agrees quite well with experimental spectra (see below). The UHB is located above 4 eV, where the t_{2g} and e_g contributions cannot be separated in energy.

The spectral density map in Fig. 2 (upper row) shows some rather well-defined band of MnO, which touches the Fermi level at the Γ point. This band is nothing else but Mn-$4s$. It can be seen from Fig. 3 that most of the Mn-$4s$ spectral weight is actually well above 5 eV. Below, there is some rather low-intensity tail, which goes through the gap between the upper Hubbard band and the Zhang–Rice band. Its intensity is at least one order of magnitude lower than the intensities of other contributions to the DOS.
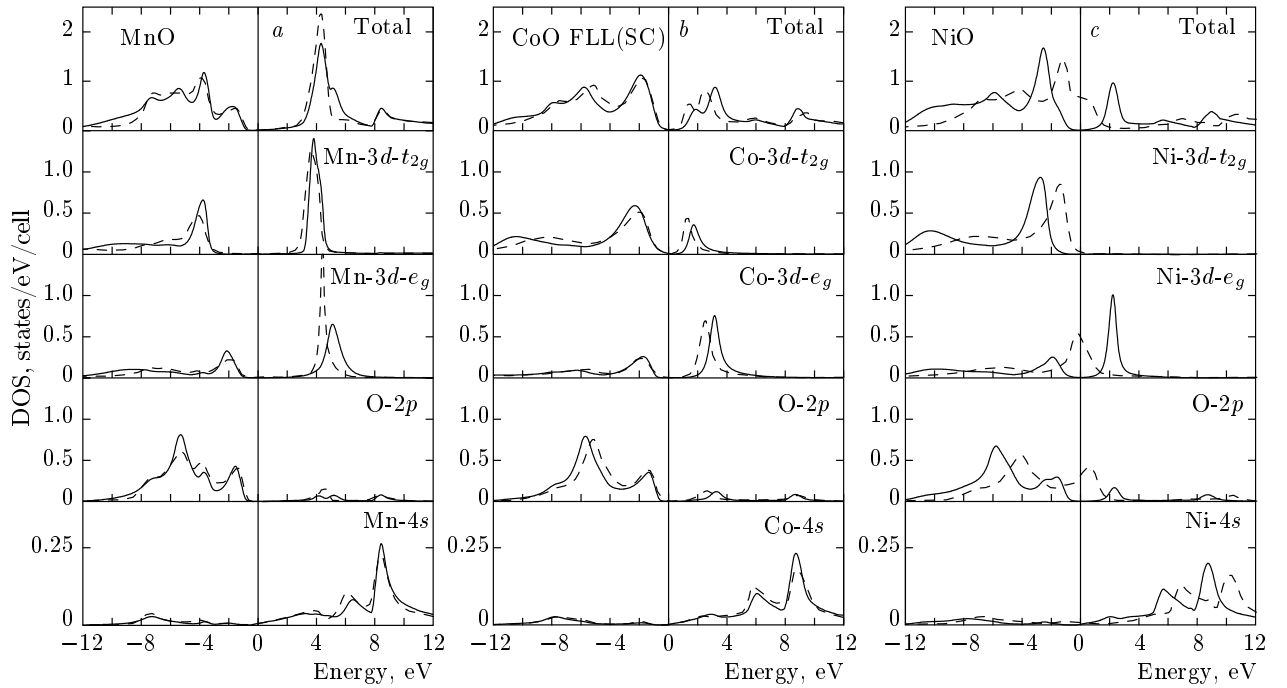
Fig. 3. Comparison of LDA+DMFT (dashed lines) and LDA'+DMFT (solid lines) densities of states for MnO (a), CoO (b), and NiO (c), with the FLL(SC) double-counting correction. The Fermi level is zero

We next consider CoO (the middle row in Fig. 2 and the middle panel in Fig. 3). We see that both LDA+DMFT and LDA'+DMFT results are quite similar. There is some difference in the UHB, where Co-3d t_{2g} and e_g contributions can now be separated, and two almost nondispersive bands around 2 eV and 3 eV above the Fermi level are clearly seen in Fig. 3. The gap between the Zhang–Rice band and the UHB is approximately 0.5 eV larger (about 4 eV) for LDA'+DMFT results.

We note that the LDA+DMFT calculation with FLL(LDA) double counting produces the metallic solution for CoO, as can be seen from Fig. 4, which qualitatively contradicts the experiments. On the contrary, the LDA'+DMFT calculation gives the correct insulating state.

We note that in both CoO and NiO, the behavior of 4s bands is similar to that discussed above for MnO. Spectral density maps in Fig. 2 show the presence of these bands within the charge-transfer gap, although the partial density of states due to these bands within the gap is almost negligible (cf. Fig. 3).

To summarize, we stress that within the LDA'++DMFT method, both MnO and CoO are consistently demonstrated to be charge-transfer insulators (in contrast to the conventional LDA+DMFT method in the

case of CoO). A similar behavior was obtained earlier for NiO in Ref. [13]. Here, we presented more complete LDA'+DMFT results for NiO, with both FLL(LDA) and FLL(SC) double-counting corrections. Conventional LDA+DMFT calculations predict NiO to be metallic in contrast to experiment, while LDA'+DMFT gives a charge-transfer insulating solution for NiO for both FLL(LDA) and FLL(SC) double-counting corrections. All other features of the NiO LDA'+DMFT band structure are quite similar to those of the MnO and CoO compounds described above.

4.4. LDA+DMFT and LDA'+DMFT optical conductivities

Metallic or insulating behavior can be explicitly demonstrated by calculations of optical conductivity. Below, we present our results for the optical conductivity behavior of MnO, CoO, and NiO in the LDA++DMFT and LDA'+DMFT approaches, which also allows us also to analyze the influence of transition-metal 4s states on dielectric properties of these oxides. We used the expression for the optical conductivity, valid in DMFT [33],
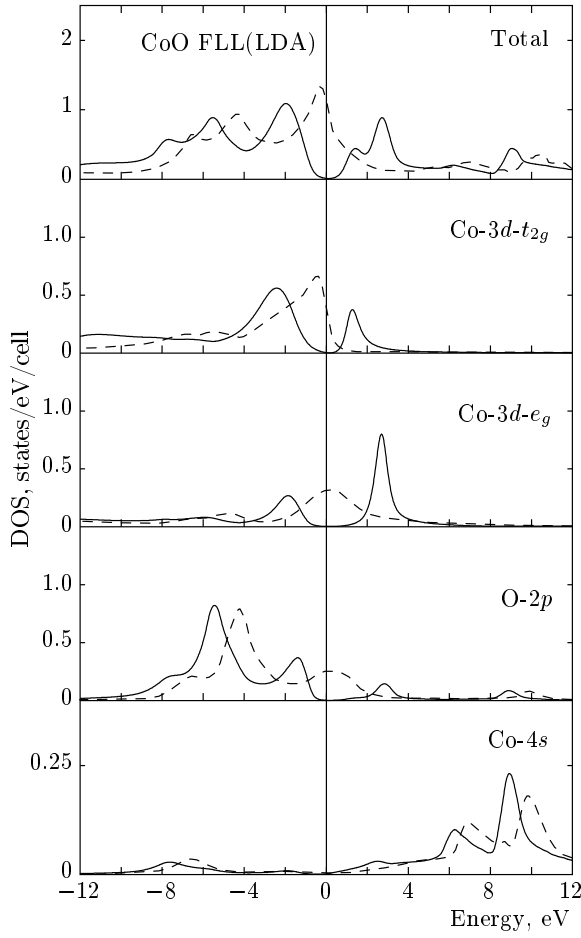
Fig. 4. Comparison of LDA+DMFT (dashed lines) and LDA′+DMFT (solid lines) calculated densities of states for CoO with the FLL(LDA) double-counting correction. The Fermi level is zero

$$\sigma_{xx}(\omega) = \frac{\pi e^2}{2\hbar a} \int\limits_{-\infty}^{\infty} d\varepsilon \frac{f(\varepsilon) - f(\varepsilon - \omega)}{\omega} \times$$

$$\times \frac{1}{N} \sum_{ij\mathbf{k}\sigma} \left(\frac{\partial \varepsilon_{\mathbf{k}}^{i}}{\partial k_x} \right) \left(\frac{\partial \varepsilon_{\mathbf{k}}^{j}}{\partial k_x} \right) A_{\mathbf{k}}^{ij}(\varepsilon) A_{\mathbf{k}}^{ji}(\varepsilon - \omega), \quad (13)$$

where e is electron charge, a is the lattice constant of the corresponding compound, $f(\varepsilon)$ is the Fermi function, $\varepsilon_{\mathbf{k}}$ is the band dispersion, and $A_{\mathbf{k}}^{ij}(\varepsilon)$ is the corresponding (LDA+DMFT or LDA′+DMFT) spectral density function matrix (i, j are the band indices). In the calculations, we found that the main contribution to optical conductivity is due to intra-orbital optical transitions. Inter-orbital optical transitions give less than 5 % of the optical conductivity intensity in the frequency range used in our calculations. We neglect possible effects due to optical matrix elements. The
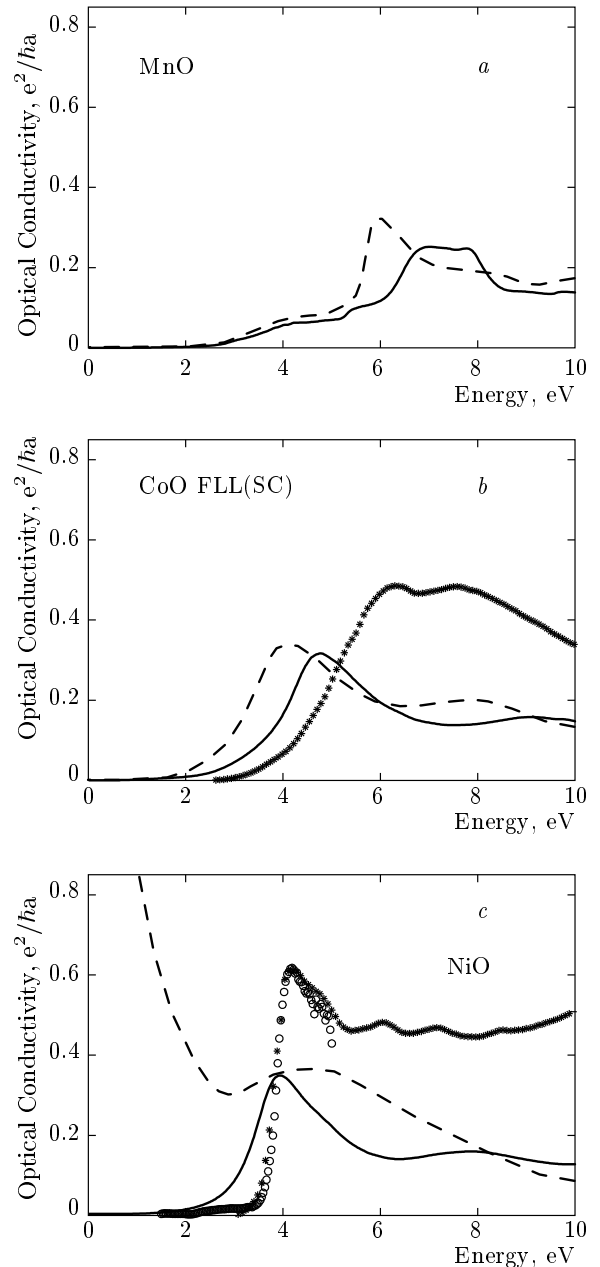
Fig. 5. Comparison of experimental (circles, stars) and calculated LDA+DMFT (dashed lines) and LDA′+ +DMFT (solid lines) optical conductivities for MnO (a), CoO (b, • — [34]), and NiO (c, ∘ — [35])

calculated theoretical curves obtained in conventional LDA+DMFT (dashed line) and LDA′+DMFT (solid line) approaches are presented in Fig. 5 for MnO (left panel), CoO (middle panel), and NiO (right panel).

We see from Fig. 5 that in the LDA′+DMFT method (solid line), all materials are insulators. Despite the presence of transition-metal 4s states close

to the Fermi level, a possible Drude peak due to these states is not observed. The conventional LDA+DMFT optical conductivity for NiO shows a typical metallic behavior, as discussed above in the context of DOS behavior.

We now compare our theoretical results with available experimental data (with the exception of MnO, where we are not aware of any experimental results) [34, 35]. In Ref. [34], only experimental data for the optical constants $n(\omega)$ and $k(\omega)$ were presented. The optical conductivity in units of $e^2/\hbar a$ (which is about $5.8 \cdot 10^3 \, \Omega^{-1} \cdot$ cm^{-1} for the selected monooxides) can be recalculated from these data as

$$\sigma(\omega) = \frac{n(\omega)k(\omega)}{2\pi}\omega\alpha^{-1}\frac{a}{c},$$

where α is fine structure constant, a is the lattice constant, and c is the speed of light. The corresponding curves are shown in Fig. 5 by stars. For NiO, there are more recent experimental data in Ref. [35], shown with circles. We observe that below the leading absorption edge for CoO and NiO, there exist rather long absorption tails with low intensity. We associate these tails with the contribution of Co and Ni $4s$ states. For NiO, the overall agreement of LDA′+DMFT results with experimental data is quite satisfactory. For CoO, the theoretical absorption edge is about 1 eV lower than the experimental one. However, this can probably be corrected by introducing a larger value of the Coulomb interaction U. A recent constrained RPA study produced it to be 10.8 eV [25], in contrast to 8 eV used in our calculations.

4.5. Comparison of LDA+DMFT and LDA′+DMFT results with X-ray experiments

We now compare our results for the DOS with XPS and BIS experiments in Refs. [36–39]. In Fig. 6, LDA+DMFT (dashed lines) and LDA′+DMFT (solid lines) valence and conduction bands spectra are directly compared with spectra for MnO (upper panel), CoO (middle panel), and NiO (lower panel). The theoretical spectra were obtained by multiplication of the DOS by the Fermi distribution and Gaussian broadening with experimental temperature and resolution.

The general structure of spectra is similar for all three compounds. From -14 eV to -4 eV, there are O-$2p$ states, then comes the lower Hubbard band at about -3 eV. On the high-energy slope of the LHB, we can see a shoulder-like structure, which is nothing else but the Zhang–Rice band. An insulating gap is near the Fermi level. The size of the gap is very well reproduced
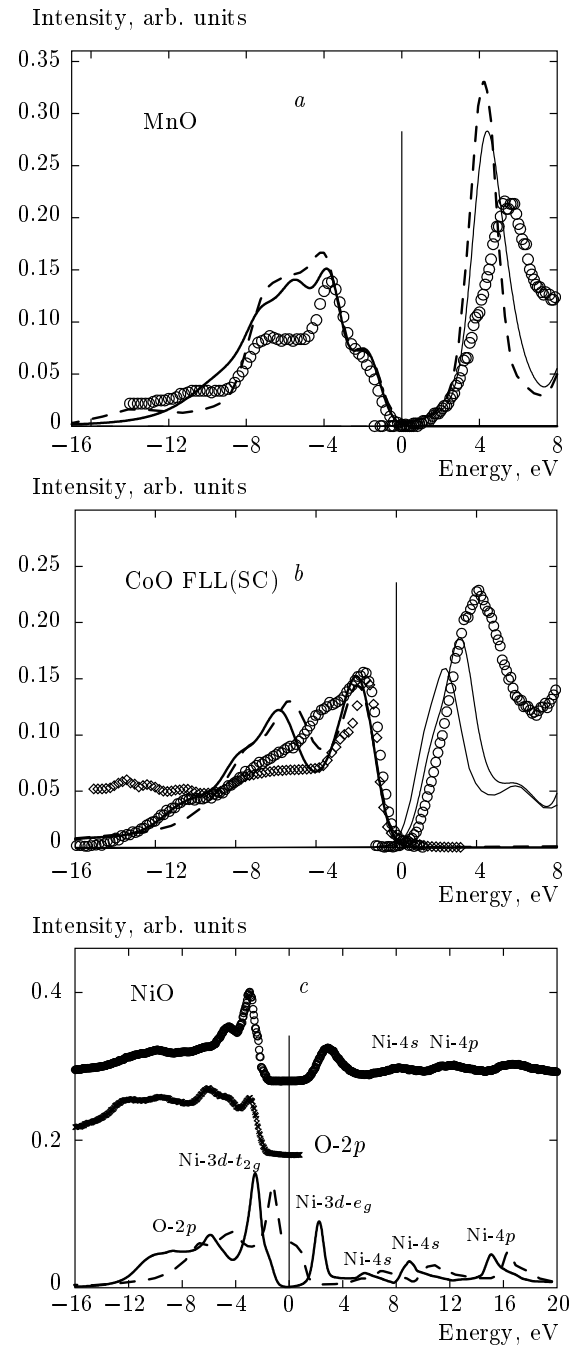
Fig. 6. Comparison of LDA+DMFT (dashed lines) and LDA′+DMFT (solid lines) spectra with XPS and BIS experimental data (circles, diamonds, crosses) for MnO (a, ○ — [36]), CoO (b, ○ — [38], ◇ — [37]), and NiO (c, ○ — [39, XPS+BIS], × — [39, XPS]). The Fermi level is zero

for MnO by both LDA+DMFT and LDA′+DMFT calculations. For CoO, it looks like the U value chosen is a bit too small (as discussed above), but LDA′+DMFT spectra gives the gap size closer to the experimental one. For NiO, the conventional LDA+DMFT calculation gives a metallic solution, while LDA′+DMFT produces a CTI solution with the correct energy gap size. Experimental positions of the upper Hubbard bands are rather well described by LDA′+DMFT. Because the experimental data for NiO go far above the Fermi level, we can identify these high-energy structures as contributions of Ni-$4s$ and Ni-$4p$ states.

In Fig. 6, the experimental conduction band low-energy threshold has a rather long low-intensity tail that goes down to the Fermi level. Therefore, there is some asymmetry of the gap. We suggest that this asymmetry of the gap originates from transition-metal $4s$ states, which touch the Fermi level from above, as described in the foregoing.

5. STRONGLY CORRELATED METALS

5.1. LDA and LDA′ band structures

Strontium vanadate $SrVO_3$ is perhaps one of the simplest paramagnetic strongly correlated metallic systems. Not surprisingly, it is widely used as a test system for various LDA+DMFT-based numerical techniques [40–43]. $SrVO_3$ has the ideal cubic perovskite structure with one d-electron in the V-$3d$ shell within a triply degenerate t_{2g} subshell. LDA and LDA′ band structure calculations are performed as described in Refs. [40–43] via the LMTO method with the von Barth–Hedin exchange correlation energy [10].

The $3d$ bands of vanadium cross the Fermi level, while oxygen $2p$ states are at -8--2 eV, i. e., much lower than the Fermi level (see Fig. 7, left panel, dashed lines). If we exclude the E_{xc}^{LDA} contribution for V-$3d$ states as described in Sec. 3, we obtain the LDA′ band structure shown in Fig. 7 (left panel, solid lines). In the LDA′ approach, similarly to Ref. [13], the energy splitting $|E_d - E_p|$ between V-$3d$ and O-$2p$ bands becomes larger than in the conventional LDA approach. Because the total number of electrons is fixed, the LDA′ increase in $|E_d - E_p|$ is related to O-$2p$ bands going down in energy by about 0.5 eV, with V-$3d$ states remaining almost unchanged. We also note that the overall band-shapes are practically unchanged in comparison with the conventional LDA bands. The same is of course true for densities of states presented in the left panel of Fig. 7.
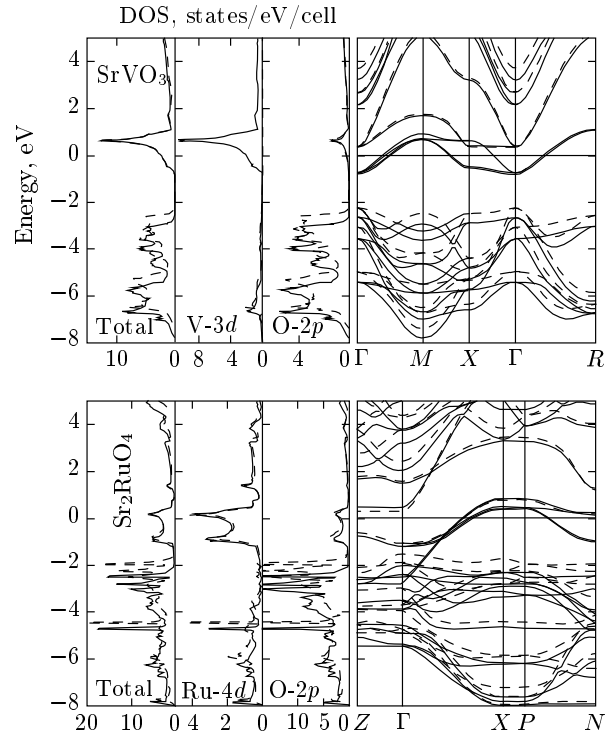

Fig. 7. LDA (dashed lines) and LDA′ (solid lines) band dispersions for $SrVO_3$ and Sr_2RuO_4. The Fermi level is zero

Another example of a paramagnetic strongly correlated metallic system widely treated by the LDA++DMFT approach is Sr_2RuO_4 with the Ru-$4d^4$ t_{2g} subshell (see Ref. [44] and the references therein). Sr_2RuO_4 is a layered perovskite with an ideal body-centered tetragonal crystal structure. For LDA and LDA′ calculations, we used settings described in Ref. [44]. LDA (dashed lines) and LDA′ (solid lines) band dispersions and DOS are plotted in Fig. 7 (right panel). The picture here is not as simple as for $SrVO_3$. The Ru-$4d$ states, crossing the Fermi level, almost preserve their energy positions and dispersions within LDA′. However LDA′ leads to the $|E_d - E_p|$ splitting because of a nonuniform narrowing of O1-$2p$ and O2-$2p$ states, together with a slight shift of O2-$2p$ states. In total, the $|E_d - E_p|$ energy splitting is about 0.5 eV larger in LDA′ than in conventional LDA.

5.2. LDA+DMFT and LDA′+DMFT DOS

In contrast to previous works (Refs. [40–44]), we here used the full TB-LMTO-ASA-calculated LDA and LDA′ Hamiltonians, not invoking any of the widely used projection techniques. In QMC calculations, the
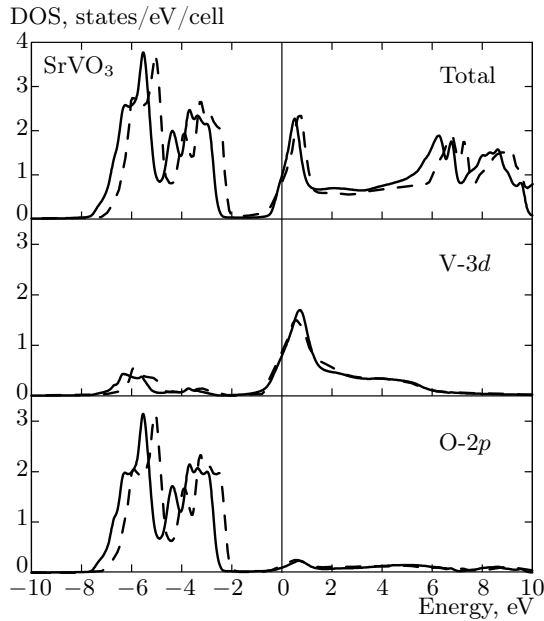
DOS, states/eV/cell

Fig. 8. Densities of states calculated with LDA+DMFT (dashed lines) and LDA'+DMFT (solid lines) for $SrVO_3$. The Fermi level is zero

DOS, states/eV/cell

Fig. 9. Densities of states calculated with LDA+DMFT (dashed lines) and LDA'+DMFT (solid lines) for Sr_2RuO_4. The Fermi level is zero

inverse temperature was taken to be $\beta = 10$ eV^{-1}, with 80 time slices for $SrVO_3$; for Sr_2RuO_4, we used $\beta = 15$ eV^{-1} with 64 time slices. The Coulomb parameters were taken to be $U = 6.0$ eV and $J = 0.7$ eV [26] for $SrVO_3$ and 3.2 eV and 0.7 eV for Sr_2RuO_4 [14]. The number of Monte Carlo sweeps was of the order of 10^6. To obtain DMFT(QMC) densities of states [31] at real energies, we again used the maximum entropy method [32]. To obtain the corresponding DMFT O-2p densities of states, the method of Pade approximants was applied to perform the analytic continuation for the DMFT self-energy from Matsubara to real frequencies, with a subsequent crosschecking of "MEM" and "Pade" DOS to ensure the quality of the restored self-energy for real frequencies.

In Figs. 8 and 9, we present the total and partial densities of states for $SrVO_3$ and Sr_2RuO_4 calculated in the conventional LDA+DMFT (dashed lines) and LDA'+DMFT (solid lines approaches). For both systems, the LDA'+DMFT results show lower positions of O-2p states in comparison with LDA+DMFT. However, for Sr_2RuO_4, this does not reduce just to a rigid shift of oxygen states by about 0.5 eV, as in the case of $SrVO_3$, but is a combination of some small shift with nonuniform narrowing of oxygen bands. For Sr_2RuO_4, only the high-energy threshold of O-2p states moves down by 0.5 eV.
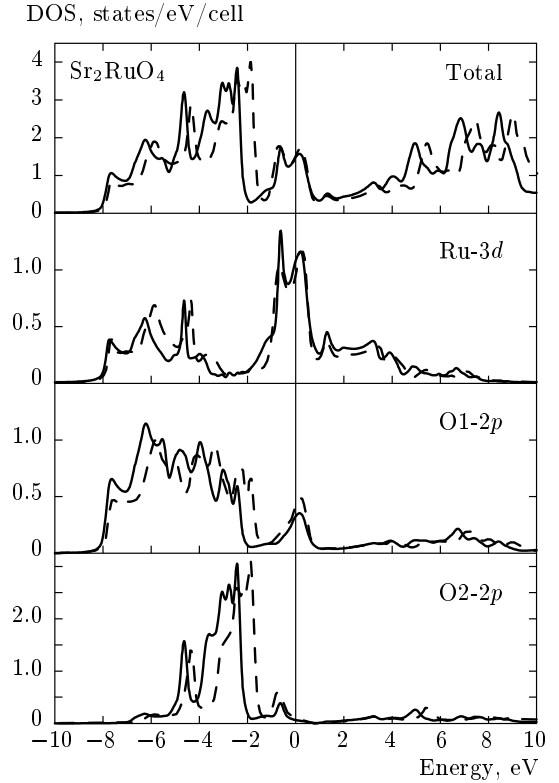
In consrast to Refs. [40–43], we observe very smooth upper and lower Hubbard bands in V-3d DOS in both calculations for $SrVO_3$ (upper panel of Fig. 8). This agrees well with the full orbital calculations reported in Ref. [26]. Also in Ref. [26] it is shown that a smaller value of E_{dc} (if E_{dc} is treated as a free parameter) moves oxygen states down in energy, which leads to better agreement with experiment (see the next paragraph).

5.3. Comparison of LDA+DMFT and LDA'+DMFT results with X-ray experiments

In Figs. 10 and 11, the LDA+DMFT (dashed lines) and LDA'+DMFT (solid lines) calculated spectra for $SrVO_3$ and Sr_2RuO_4 are drawn. To obtain theoretical spectra from the total DOS, Gaussian broadening to simulate the experimental resolution and Lorentzian broadening to simulate lifetime effects, together with multiplication with the Fermi distribution function, were performed as described elsewhere [40–44]. In the figures, emission (left side) and absorption (right side) spectra are plotted.
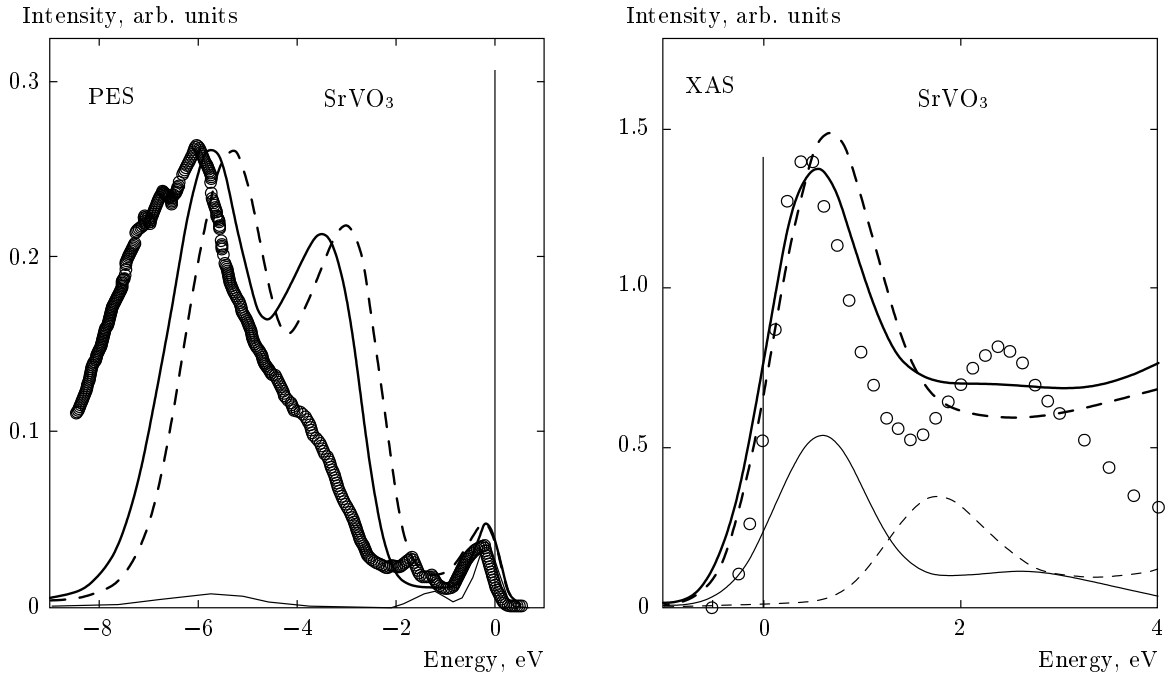
Fig. 10. Comparison of LDA+DMFT (dashed lines) and LDA'+DMFT (solid lines) calculated spectra for $SrVO_3$ with experimental data ($\bullet$ — [41], $\circ$ — [45]). Thin lines shows the LDA'+DMFT t_{2g} (solid line) and e_g (dot-dash line) V-$3d$ contributions. The Fermi level is zero

For both systems, we have reasonable agreement with experimental data (circles) for valence and conducting bands [41, 45–47]. But the strength of the quasiparticle peak is somewhat overestimated for the valence band and underestimated for the conduction band in both LDA+DMFT and LDA'+DMFT methods. The LDA'+DMFT results give a slightly better energy position of O-$2p$ states in comparison with LDA+DMFT. In general, the results obtained by the LDA'+DMFT method are in agreement with the previous LDA+DMFT works (see Refs. [40–44]).

To demonstrate the presence of the well-known lower Hubbard band at -1.5 eV for $SrVO_3$ [40–43] the V-$3d$ t_{2g} contribution is shown by the thin line in the left panel of Fig. 10. In Fig. 10 (right panel) for $SrVO_3$, the LDA'+DMFT calculation shows a rather broad shoulder around 2.5 eV instead of the upper Hubbard band. This shoulder is formed by the t_{2g} (solid thin line) and e_g (dot-dashed thin line) V-$3d$ contributions that corresponds to previous works [40–43]. However, the e_g subband is also modified by correlations in our case. It is shifted by about 1 eV (as should be the case for completely empty states) and it has a smaller width compared to the LDA one. For Sr_2RuO_4, it is known that correlations lead to formation of a lower-Hubbard-band satellite near -3 eV [44]. This satellite

is also seen in the LDA'+DMFT results in the right panel of Fig. 11 and is formed essentially by Ru-$4d$ t_{2g} states (thin line).

6. CONCLUSION

This work continues our research of the double-counting problem arising within the LDA+DMFT computational scheme. The problem appears because some portion of local electron–electron interaction is already present in LDA calculations. Because DMFT method gives an exact local solution of the Hubbard-like model, double counting between the LDA and DMFT local electronic interactions must be avoided. Despite 15 years of developing the LDA+DMFT method, there is still no unique definition of this double-counting term. This is because the LDA contribution to the exchange correlation energy has no diagrammatic expression. Several different *ad hoc* definitions that are currently available work well only in some particular cases, for some particular compounds. Sometimes the LDA+DMFT solution is wrong even qualitatively if the double-counting term is chosen not carefully enough. To overcome this problem, we proposed a consistent LDA'+DMFT approach [13]. It uses a natural as-
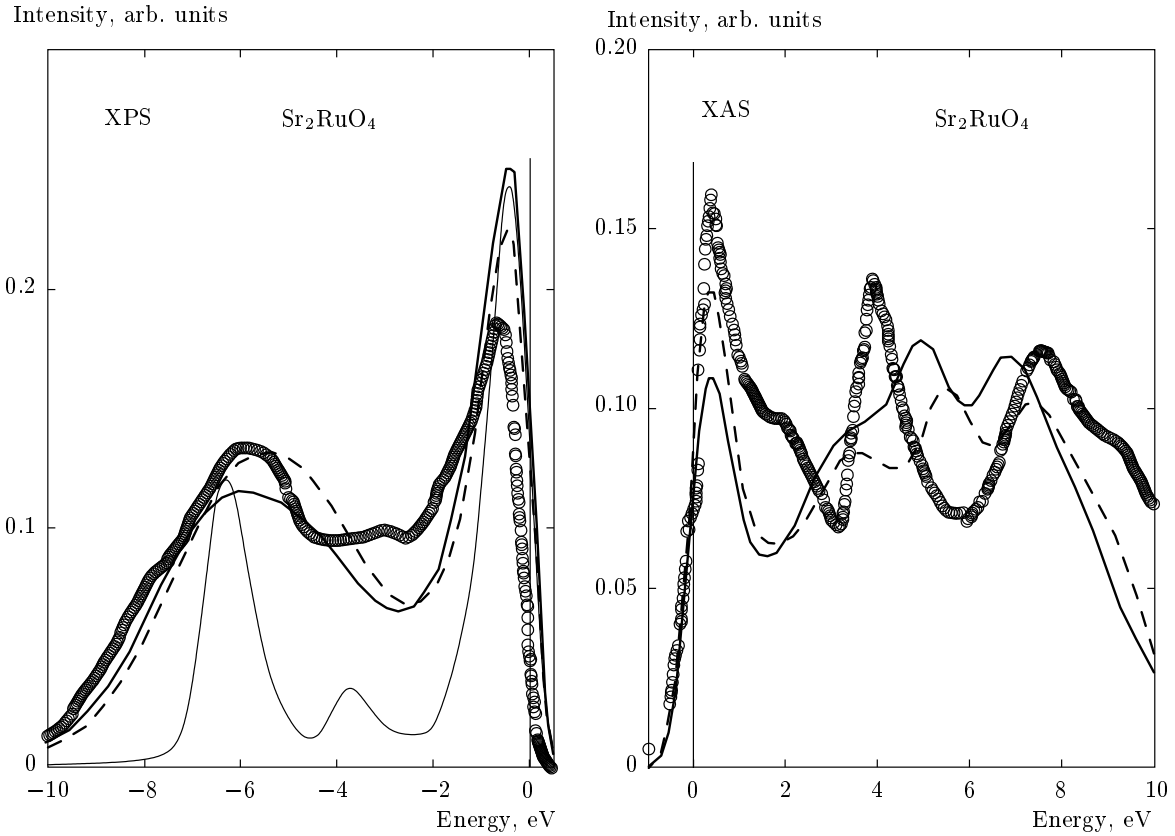
Fig. 11. Comparison of LDA+DMFT (dashed lines) and LDA′+DMFT (solid lines) calculated spectra for Sr_2RuO_4 with experimental data (● — [46], ○ — [47]). Thin line shows the LDA′+DMFT t_{2g} Ru-$4d$ contribution. The Fermi level is zero

sumption of the explicit exclusion of the LDA exchange correlation potential for correlated electronic shells because exchange-correlation effects are anyway taken into account later by the DMFT computation. Then the local interactions left out for correlated states in the LDA′ computation are only Hartree ones. After that, the corresponding double-counting term of the LDA′+DMFT Hamiltonian must be consistently taken in the local Hartree form (FLL form).

In this paper, we present an extensive LDA′+ +DMFT investigation of typical representatives of two wide classes of strongly correlated systems in the paramagnetic phase: strongly correlated metals ($SrVO_3$ and Sr_2RuO_4) and charge-transfer insulators (MnO, CoO, and NiO). For strongly correlated metals, where double counting is not that severe, the LDA′+DMFT method agrees well with traditional LDA+DMFT results with an FLL double-counting type. The LDA′+DMFT method gives a slightly better position of O-$2p$ states in comparison with experiment. The LDA′+DMFT results for charge-transfer insulators MnO, CoO, and NiO

are more interesting. CoO and NiO systems are found to be metals in the conventional LDA+DMFT calculations, while LDA′+DMFT gives a proper insulating solution. Transition-metal $4s$-states missed in previous LDA+DMFT works on these monooxides are found to be responsible for the charge gap asymmetry around the Fermi level.

Finally, we can conclude that the proposed consistent LDA′+DMFT method works well for both metallic and insulating systems. We believe that our LDA′+DMFT method provides a reasonable parameter-free treatment of the double-counting problem.

mesoscopic and disordered structures" (12-П-2-1002) and of the Physics Division of RAS "Strongly correlated electrons in solids and structures" (012-Т-2-1001). N. S. P. acknowledges the support of the Dynasty Foundation and the International Center of Fundamental Physics in Moscow.

REFERENCES

1. V. I. Anisimov, A. I. Poteryaev, M. A. Korotin, A. O. Anokhin, and G. Kotliar, J. Phys.: Cond. Matter **9**, 7359 (1997).

2. A. I. Lichtenstein and M. I. Katsnelson, Phys. Rev. B **57**, 6884 (1998).

3. I. A. Nekrasov, K. Held, N. Blümer et al., Eur. Phys. J. B **18**, 55 (2000).

4. K. Held, I. A. Nekrasov, G. Keller et al., Psi-k Newsletter **56**, 65 (2003).

5. K. Held, I. A. Nekrasov, N. Blümer, V. I. Anisimov, and D. Vollhardt, Int. J. Mod. Phys. B **15**, 2611 (2001); K. Held, I. A. Nekrasov, G. Keller et al., in: *Quantum Simulations of Complex Many-Body Systems: From Theory to Algorithms*, ed. by J. Grotendorst, D. Marks, and A. Muramatsu, NIC Series Vol. 10 (2002), p. 175; A. I. Lichtenstein, M. I. Katsnelson, and G. Kotliar, in: *Electron Correlations and Materials Properties, 2nd ed.*, ed. by A. Gonis, N. Kioussis, and M. Ciftan, Kluwer Academic/Plenum (2002), p. 428.

6. G. Kotliar, S. Y. Savrasov, K. Haule et al., Rev. Mod. Phys. **78**, 865 (2006).

7. V. I. Anisimov and Yu. A. Izyumov, *Electronic Structure of Strongly Correlated Materials*, Berlin-Heidelberg, Springer (2010).

8. B. Amadon, J. Phys.: Condens. Matter **24**, 075604 (2012).

9. R. O. Jones and O. Gunnarsson, Rev. Mod. Phys. **61**, 689 (1989).

10. L. Hedin and B. Lundqvist, J. Phys. C: Sol. St. Phys. **4**, 2064 (1971); U. von Barth and L. Hedin, J. Phys. C: Sol. St. Phys. **5**, 1629 (1972).

11. D. M. Ceperley and B. J. Alder, Phys. Rev. Lett. **45**, 566 (1980).

12. M. B. Zölfl, Th. Pruschke, J. Keller et al., Phys. Rev. B **61**, 12810 (2000).

13. I. A. Nekrasov, N. S. Pavlov, and M. V. Sadovskii, Pis'ma v ZhETF **95**, 659 (2012); arXiv:1204.2361.

14. V. I. Anisimov, J. Zaanen, and O. K. Andersen, Phys. Rev. B **44**, 943 (1991); V. I. Anisimov, F. Aryasetiawan, and A. I. Lichtenstein, J. Phys. Cond. Matter **9**, 767 (1997).

15. M. T. Czyżyk and G. A. Sawatzky, Phys. Rev. B **49**, 14211 (1994).

16. O. Gunnarsson, O. K. Andersen, O. Jepsen, and J. Zaanen, Phys. Rev. B **39**, 1708 (1989).

17. F. Aryasetiawan, M. Imada, A. Georges et al., Phys. Rev. B **70**, 195104 (2004); I. V. Solovyev and M. Imada, Phys. Rev. B **71**, 045103 (2005).

18. J. Kunes, V. I. Anisimov, S. L. Skornyakov, A. V. Lukoyanov, and D. Vollhardt, Phys. Rev. Lett. **99**, 156404 (2007); J. Kunes, V. I. Anisimov, A. V. Lukoyanov, and D. Vollhardt, Phys. Rev. B **75**, 165115 (2007).

19. V. I. Anisimov, I. V. Solovyev, M. A. Korotin, M. T. Czyżyk, and G. A. Sawatzky, Phys. Rev. B **48**, 16929 (1993).

20. J.-X. Zhu, P. H. Tobash, E. D. Bauer et al., Europhys. Lett. **97**, 57001 (2012).

21. I. Leonov, A. Poteryaev, V. Anisimov, and D. Vollhardt, Phys. Rev. Lett. **106**, 106405 (2011).

22. V. Anisimov, A. Belozerov, A. Poteryaev, and I. Leonov, arXiv:1204.1636.

23. A. I. Lichtenstein, M. I. Katsnelson, and G. Kotliar, Phys. Rev. Lett. **87**, 067205 (2001); M. I. Katsnelson and A. I. Lichtenstein, Eur. Phys. J. B **30**, 9 (2002).

24. F. Aryasetiawan, S. Biermann, and A. Georges, in *Correlation Spectroscopy of Surfaces, Thin Films, and Nanostructures*, Wiley-VCH Verlag GmbH & Co. KGaA, ed. by J. Berakdar and J. Kirschner (2004), p. 1, ISBN: 3-527-40477-5, arXiv:0401626.

25. J. Kunes, V. Krapek, and A. V. Kozhevnikov, arXiv: 1202.0110.

26. B. Amadon, F. Lechermann, A. Georges, F. Jollet, T. O. Wehling, and A. I. Lichtenstein, Phys. Rev. B **77**, 205112 (2008).

27. M. Karolak, G. Ulm, T. Wehling et al., J. Electr. Spectr. Relat. Phenom. **181**, 11 (2010).

28. K. Held, Adv. Phys. **56**, 829, 862 (2007).

29. K. Held, C. Taranto, G. Rohringer, and A. Toschi, *Hedin Equations*, GW, GW+DMFT, *and All That in The* LDA+DMFT *Approach to Strongly Correlated Materials — Lecture Notes of the Autumn School 2011 Hands-on* LDA+DMFT; ed. by E. Pavarini, E. Koch, D. Vollhardt, and A. Lichtenstein, FZ Julich GmbH (2011) [arxiv.org/abs/1109.3972].

30. O. K. Andersen, Phys. Rev. B **12**, 3060 (1975); O. K. Andersen and O. Jepsen, Phys. Rev. Lett. **53**, 2571 (1984).

31. J. E. Hirsch and R. M. Fye, Phys. Rev. Lett. **56**, 2521 (1986); M. Jarrell, Phys. Rev. Lett. **69**, 168 (1992); M. Rozenberg, X. Y. Zhang, and G. Kotliar, Phys. Rev. Lett. **69**, 1236 (1992); A. Georges and W. Krauth, Phys. Rev. Lett. **69**, 1240 (1992); M. Jarrell, in *Numerical Methods for Lattice Quantum Many-Body Problems*, ed. by D. Scalapino, Addison Wesley (1997).

32. M. Jarrell and J. E. Gubernatis, Phys. Rep. **269**, 133 (1996).

33. Th. Pruschke, M. Jarrel, and J. K. Freericks, Adv. Phys. **44**, 187 (1995).

34. R. J. Powell and W. E. Spicer, Phys. Rev. B **2**, 2182 (1970).

35. Y. K. Seo, D. J. Lee, and Y. S. Lee, J. Korean Phys. Soc. **55**, 129 (2009).

36. J. van Elp, R. H. Potze, H. Eskes, R. Berger, and G. A. Sawatzky, Phys. Rev. B **44**, 1530 (1991).

37. S. Hufner and G. K. Wertheim, Phys. Rev. B **8**, 4857 (1973).

38. J. van Elp, J. L. Wieland, H. Eskes et al., Phys. Rev. B **44**, 6090 (1991).

39. G. A. Sawatzky and J. W. Allen, Phys. Rev. Lett. **53**, 2339 (1984).

40. A. Sekiyama, H. Fujiwara, S. Imada et al., Phys. Rev. Lett. **93**, 156402 (2004).

41. V. I. Anisimov, D. E. Kondakov, A. V. Kozhevnikov et al., Phys. Rev. B **71**, 125119 (2005).

42. I. A. Nekrasov, G. Keller, D. E. Kondakov et al., Phys. Rev. B **72**, 155106 (2005).

43. I. A. Nekrasov, K. Held, G. Keller et al., Phys. Rev. B **73**, 155112 (2006).

44. Z. V. Pchelkina, I. A. Nekrasov, Th. Pruschke et al., Phys. Rev. B **75**, 035122 (2007).

45. I. H. Inoue, I. Hase, Y. Aiura et al., Physica C **235**, 1007 (1994).

46. T. Yokoya, A. Chainani, T. Takahashi et al., Phys. Rev. B **53**, 8151 (1996).

47. E. Z. Kurmaev, S. Stadler, D. L. Ederer et al., Phys. Rev. B **57**, 1558 (1998).